Astronomy & Astrophysics manuscript no. output
May 9, 2026

SPATO: A-F variable stars catalogue within PLATO first field of view LOPS2

Carlos C. Camino Mesa[1], A. García Hernández[1], J.C. Suárez[1], Giovanni M. Mirouh[1], and A. Florido-Tomé[1]

Universidad de Granada, Dept. Física Teórica y de Cosmos, Fuentenueva Campus, E-18007, Granada, Spain
e-mail: carlosccamino@ugr.es

May 9, 2026

ABSTRACT

Context. Space-based photometry has enabled major advances in asteroseismology, particularly for intermediate-mass A-F type stars located at the intersection of the main sequence and the classical instability strip. These stars, including δ Scuti, γ Dor, and roAp variables, exhibit a wide range of pulsation regimes and excitation mechanisms, but their big scale characterization is often limited by absence of frequencies of oscillations in the majority of catalogues.
Aims. We present SPATO, a catalogue of stellar parameters and pulsation frequencies for A–F type stars in the PLATO LOPS2 field, and assess the validity of classical classification schemes based on frequency domains.
Methods. TESS light curves were homogeneously processed and analysed to extract independent frequencies. Stellar parameters from TESS and Gaia were combined to define an enriched sample. Pulsators were classified according to their frequency content.
Results. The classical separation at 5 c/d does not produce a clear distinction between δ Scuti and γ Dor stars in the HR diagram. Instead, the period–luminosity diagram reveals two main populations separated by a low-density region, which we propose as an alternative observational discriminator. Radial modes, particularly the fundamental and first overtone, follow well-defined relations, while higher overtones show larger dispersion. We find linear relations between observational $\nu_{\rm A}$ and estimations of R and $\log g$, which could help in spectroscopic degeneracy when determining the latter.
Conclusions. SPATO provides a large, homogeneous dataset that highlights the limitations of classical classifications and supports the use of period–luminosity relations as complementary tools, paving the way for future studies with PLATO.

1. Introduction

Space missions such as MOST (Microvariability and Oscillations of STars; Walker et al. 2003), CoRoT (Baglin et al. 2006), Kepler (Borucki et al. 2010), and more recently TESS (Transiting Exoplanet Survey Satellite; Ricker et al. 2014) have enabled highly precise stellar studies through the analysis of oscillation frequencies in space-based photometry, demonstrating the strong potential of asteroseismology. Intermediate-mass pulsating stars, of spectral types A–F (with masses between $1.3M_\odot$ and $3M_\odot$ on the main sequence) are of particular interest due to their diversity in oscillation properties, internal structure, and rotation (Aerts et al. 2010). This group includes roAp, γ Dor and δ Scuti stars, all of which occupy a similar region in the Hertzsprung–Russell (HR) diagram at the intersection of the main sequence and the classical instability strip.

δ Scuti stars are characterized by the presence of tens to hundreds of oscillation frequencies (e.g. Breger et al. 2005), providing rich asteroseismic information. They typically pulsate in low-order radial and non-radial p modes within the frequency range 5–80 c/d (Uytterhoeven et al. 2011). These stars often overlap with the less massive γ Dor stars, which pulsate predominantly in high-order g modes with frequencies below $\sim$ 5 c/d, probing deeper stellar layers (Dupret et al. 2005). The presence of hybrid pulsators (Grigahcène et al. 2010) in this overlapping region makes them particularly valuable for studying mode excitation mechanisms. δ Scuti stars are driven by the opacity (κ) mechanism in the He II ionization zone (Breger & Montgomery 2000), and γ Dor stars are thought to pulsate due to convective flux blocking (Dupret et al. 2005; Guzik et al. 2000). Hybrid stars exhibit both types of modes simultaneously, but the relation between their excited g modes and the κ mechanism is not fully understood (Xiong et al. 2016). In contrast, roAp stars show high-overtone p modes with periods of a few minutes (Kurtz 1982), and are characterized by strong magnetic fields and chemically peculiar atmospheres (e.g. Hubrig et al. 2005).

The upcoming European Space Agency mission PLATO (PLAnetary Transits and Oscillations of stars; Rauer et al. 2025) will represent a major step forward in the characterization of this heterogeneous group. Although primarily designed for the detection of exoplanets around solar-like stars, PLATO will provide 24 normal cameras (N-CAMs) and 2 fast cameras (F-CAMs), delivering cadences of $\Delta t = 25$ s and $\Delta t = 2.5$ s, respectively. These cadences will allow the exploration of a much broader range of pulsation frequencies due to the high Nyquist frequency, $\mathrm{f_{Ny}} = 1/(2\Delta t)$. In addition, the long observing campaigns in the Long-duration Observation Phase (LOP) will improve both the signal-to-noise ratio and the frequency resolution, the latter given by the Rayleigh frequency $\mathrm{f_R} = 1/T$ with T as the total timespan of the observation. These improvements enable the detection of lower-amplitude modes and closer frequencies (VanderPlas 2018). The availability of color photometry from 2 cameras, not present in TESS,

will provide additional constraints and data for the study of A–F pulsators (Garrido et al. 2004; Zwintz et al. 2019).

PLATO therefore offers the possibility to improve our understanding of intermediate-mass pulsating stars, such as roAp, δ Scuti and γ Dor variables. In this context, we present SPATO (Survey of PLATO A-Type stars Oscillation frequencies), a catalogue of main-sequence and early post-main-sequence A-F-type stars focused on the first long-duration pointing, LOPS2 (Nascimbeni et al. 2025). SPATO combines stellar parameters from the TESS Input Catalogue (TIC; Stassun et al. 2019) and Gaia DR3 (Gaia Collaboration et al. 2023), open cluster memberships, and oscillation frequencies extracted from TESS light curves, together with a classification based on their frequency content. This homogeneous compilation makes SPATO a valuable resource for large-scale studies of A-F pulsating stars, including precise sample selection, big-scale frequency analysis, and amplitude characterization. The catalogue is intended as a preparatory tool for future PLATO observations and as a resource to investigate the observational properties and classification of A–F pulsators.

In this work, we use SPATO to focus on δ Scuti and γ Dor stars, specifically on the impact of their pulsation frequencies on their position in the HR diagram, the revision of classical classification schemes, the pulsator fraction, and the period–luminosity relation of δ Scuti stars.

2. Sample Selection

We obtained the initial target list from TIC v8.1 which covers the entire LOPS2 region, and includes 90% of the southern TESS continuous viewing zone (Nascimbeni et al. 2025).

The selection of sources from the TIC was performed through a query to MAST[1] (Mikulski Archive for Space Telescopes) using the *Python* package *astroquery*[2] (Ginsburg et al. 2019). The query parameters are listed in Table 1.

The query consists of three parts. The first is spatial, defined by constraints on galactic longitude (ℓ) and latitude (b) to encompass the LOPS2 region, since selecting the exact field with a single query is not straightforward. The second is instrumental, based on the nominal capability of PLATO for sources brighter than $V = 16$ (Rauer et al. 2025; Nascimbeni et al. 2025). The third part is physical, applying constraints on the effective temperature ($T_{\rm eff}$) and the surface gravity ($\log g$). This last part allows us to target the region of the ($\log g$-$T_{\rm eff}$) diagram where p- and g-mode pulsators are expected (e.g. Uytterhoeven et al. 2011; Bowman & Kurtz 2018).

Finally, to refine the spatial selection and retain only objects within LOPS2, the resulting sample was cropped to match the correct footprint using a LOPS2 MOC[3] (Multi-Order Coverage Map), which defines our "initial sample".

Although the full initial sample was processed and is available, SPATO includes a subsample referred to as the "enriched sample". In addition to the conditions listed in Table 1, this subsample satisfies the constraints given in Table 2 for Gaia DR3. This additional constraint on $T_{\rm eff}$ and luminosity L, obtained from an independent mission (Gaia), provides a higher level of consistency in the determination of stellar parameters for these stars.

[1] https://mast.stsci.edu/api/v0/

[2] https://github.com/astropy/astroquery

[3] Publicly available on Zenodo: https://zenodo.org/records/14720127

Table 1. TESS parameter constraints for the MAST query used to retrieve the initial target list.

Parameter	From	To
ℓ (deg)	214.9975	296.8775
b (deg)	-49.24864	0
$T_{\rm eff}$ (K)	6500	9000
$\log g$ (dex)	3.5	4.2
V (mag)	–	16

The selected ranges are motivated by the region of the HR diagram where p- and g-mode A-type pulsators are typically found (e.g. Aerts et al. 2010; Murphy et al. 2019). In this sense, the enriched sample represents a set of stars with more and better constrained parameters, which are also expected to have a higher probability of pulsation based on their position in the ($\log g$-$T_{\rm eff}$) diagram from TESS and in the HR diagram from Gaia.

Table 2. Gaia parameter constraints used for the query that was crossmatched with the initial sample to retrieve the enriched sample. "Star or binary prob." refers to the probability of the target for being a star or a binary system.

Parameter	From	To
ℓ (deg)	214.9975	296.8775
b (deg)	-49.24864	0
$T_{\rm eff}$ (K)	6500	9000
L ($L_\odot$)	3	33
Star or binary prob.	99%	100%

For validation purposes of the pulsator classification, we cross-matched the enriched sample with the Variable Star Index (VSX; Watson et al. 2006) within the LOPS2 region to identify already catalogued variable stars.

Finally, using the open clusters catalogue by Hunt & Reffert (2024), we performed a TAP Vizier (Ochsenbein et al. 2000) query to retrieve the open clusters located within LOPS2 constraining only by the galactic coordinates given in Table 1 and Table 2. The results were cross-matched with initial sample.

3. Stellar parameters

3.1. Data Sources

The data presented in this catalogue belongs to 3 different sources, when available: TIC stellar parameter estimates, Gaia DR3 stellar parameter estimates, and TESS light curves processing.

The TIC stellar parameters are listed in Table A.1. Surface gravity ($\log g$) should be treated with caution, as it is derived from TICv8 own internal calculations of stellar masses and radii to ensure internal consistency, even if spectroscopic measurements were available. By contrast, the effective temperature is determined from spectroscopy whenever possible, or otherwise from an empirical relation that scales with Gaia's colour index as ($G_{BP} - G_{RP}$) color. Metallicity [M/H], as for $T_{\rm eff}$, is a spectroscopic measure when available, but in this case it is for completeness

since it is not used in any relation to derive stellar parameters. These and the rest of the caveats are detailed in Stassun et al. (2019).

For the enriched sample, we extracted the Gaia DR3 stellar parameters presented in Table A.2. We included stellar parameters from the methods that covered most of our sample, namely the General Stellar Parametrizer from Photometry (*GSP-Phot*; Andrae et al. 2023) and the Final Luminosity Age Mass Estimator (*FLAME*; Creevey et al. 2023). Nevertheless, users should be cautious when using the values given by these methods. For instance, *GSP-Phot* tends to poorly estimate [M/H], overestimate $T_{\rm eff}$ for stars located in the galactic plane, and may underestimate distances when parallax quality is poor (see online documentation[4]). *GSP-Phot* does not correct for certain effects in stars with effective temperatures above 7500 K. Therefore, in the temperature range of 7500–9000 K, we adopted the $T_{\rm eff}$ values provided by the Extended Stellar Parametrizer for Hot Stars (*ESP-HS*[5]). On the other hand, *FLAME* results for age, mas,s and evolution stage are based on comparisons with solar metallicity stellar models, and their uncertainties are generally underestimated (see online documentation [6]).

As a third input, the light curves included in SPATO were selected from all available TESS data products by prioritizing those with the shortest cadence and, secondarily, those with the largest number of consecutive sectors. Prioritizing shorter cadences over a longer temporal baseline provides a wider spectral window, i.e. a higher Nyquist frequency $f_{\rm Ny}$, which is required to cover the expected pulsation ranges: $\approx [5, 80]$ c/d for δ Scuti stars, $\approx [0.33, 5]$ c/d for γ Doradus stars (Grigahcène et al. 2010), and $\approx [61, 307]$ c/d for roAp stars (Holdsworth et al. 2024).

Conversely, maximizing the number of consecutive sectors, i.e. greater T permits resolving more frequencies by reducing $f_{\rm R}$. Consecutive sectors preserve phase coherence, which is essential for the correct frequency analysis of non-stochastically driven pulsations.

Among the selected light curves, we also prioritized the processing pipeline when multiple products shared the same cadence and number of consecutive sectors. First, we favored the TESS Asteroseismic Science Operations Center (TASOC; Handberg et al. 2021; Lund et al. 2021), as it is specifically designed for asteroseismic analysis. Second in priority is the TESS Science Processing Operations Center pipeline (SPOC; Caldwell et al. 2020), which processes the data directly from the TESS full-frame images (FFIs). The MIT Quicklook Pipeline (QLP; Huang et al. 2020a,b; Kunimoto et al. 2021) is ranked third; although it also uses TESS FFIs, it relies on TIC-based magnitude estimates for its corrections, such that later TIC updates may not be reflected in subsequent QLP versions. Next, the TESS-Gaia Light Curve pipeline (TGLC; Han & Brandt 2023) is considered, which likewise uses FFIs and incorporates Gaia DR3 priors to identify contaminating sources. Finally, light curves from either GSFC-ELEANOR-LITE or CDIPS are retrieved when none of the aforementioned pipelines are available.

Each of these pipelines provides different levels of flux post-processing; the selected products are listed in Table A.3.

3.2. Data comparison

The initial sample resulted in 281,279 targets, which are plotted in the left panel of Figure 1 while the enriched sample (right panel) is constituted by 125,025 targets. We considered the brightest stars as those with V < 6, for which we report primary identifiers. Since the upper limit in brightness for PLATO N-CAMs is $V = 8$, these targets will cause PLATO N-CAMs to saturate, but F-CAMs will be able to obtain data for these objects since they will be able to observe up to $V = 4.5$ (Rauer et al. 2025).

In addition to identifying the brightest targets, we characterize the overall stellar sample by presenting the distributions of the main parameters provided by TESS in Fig. 2. These are compared with the corresponding estimates from Gaia, and this comparison is therefore limited to the enriched sample. It is worth noting that not all stars in the enriched sample have the stellar parameters listed in Table A.2 well determined. As a result, the number of stars included in each distribution varies from one panel to another, although the overall trends remain valid for our analysis.

The stellar parameter distributions indicate that we are effectively probing the fainter part of the classical instability strip, where we can expect to find pulsators such as δ Scuti, γ Doradus, or roAp stars.

The effective temperature distributions show peaks around 6500 K in both sources (TIC v8 and Gaia DR3), although Gaia tends to yield greater values than TESS for $T_{\rm eff} < 7500$ K, consistent with the caveats noted in Sect. 3.1. The discontinuity at 7500K is due to the change of source from *GSP-Phot* to *ESP-HS* for the effective temperature.

TESS radius and $T_{\rm eff}$ distributions have similar behaviour, highlighting its derivation via the Stefan–Boltzmann relation and the strong correlation with $T_{\rm eff}$. TESS M and R peak at $\sim 1.4\,{\rm M}_\odot$, and at $\sim 1.9\,{\rm R}_\odot$, respectively. On the other hand, Gaia's *FLAME* pipeline mass and radius distributions are smoother and suggest slightly more massive yet smaller stars overall.

Surface gravity distributions are also similar, but the TESS sample is sharply truncated at the imposed constraint, while Gaia extends up to $\log g = 4.5$ dex. Nevertheless, both concentrate in the same region, and the Gaia extension represents fewer than 25% of the targets.

Luminosity distributions are broadly consistent, although Gaia tends to concentrate sources at lower luminosities, which suggests a general overestimation of L in TIC.

Metallicities from TIC are systematically higher and, when available from spectroscopy, more reliable. In contrast, Gaia metallicities are inferred from model fits and are generally considered unreliable for detailed analysis, as also noted in the mission documentation. Despite this, both methods point towards subsolar metallicity stars in more than 75% of our sample.

The projected rotational velocity, $v \cdot \sin i$, is available for 7,102 out of the 125,025 targets contained in the enriched sample. This parameter is provided by the *ESP-HS* module

[4] https://gea.esac.esa.int/archive/documentation/GDR3/Data_analysis/chap_cu8par/sec_cu8par_apsis/ssec_cu8par_apsis_gspphot.html

[5] https://gea.esac.esa.int/archive/documentation/GDR3/Data_analysis/chap_cu8par/sec_cu8par_apsis/ssec_cu8par_apsis_esphs.html

[6] https://gea.esac.esa.int/archive/documentation/GDR3/Data_analysis/chap_cu8par/sec_cu8par_apsis/ssec_cu8par_apsis_flame.html

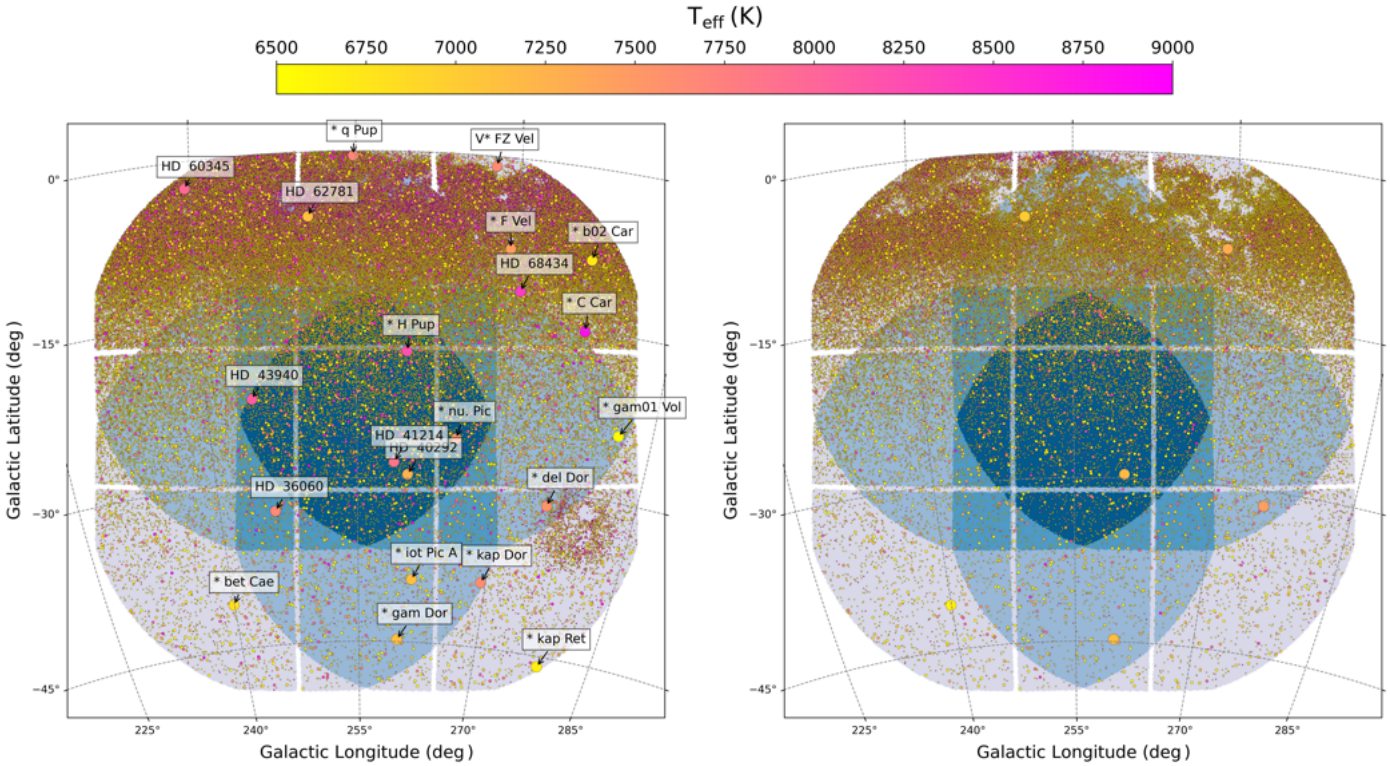

Fig. 1. Targets in LOPS2 field of view. TESS effective temperature is color coded and magnitude in V band is proportional to the point area as follows: 1.4 when V $\geq$ 10, 7 when 6 $\geq$ V $\geq$ 10 and 100 when V $<$ 6. *Left panel*: Initial sample (see definition at 2). *Right Panel*: TESS targets with additional Gaia data, called in the text enriched sample (see Section 2).

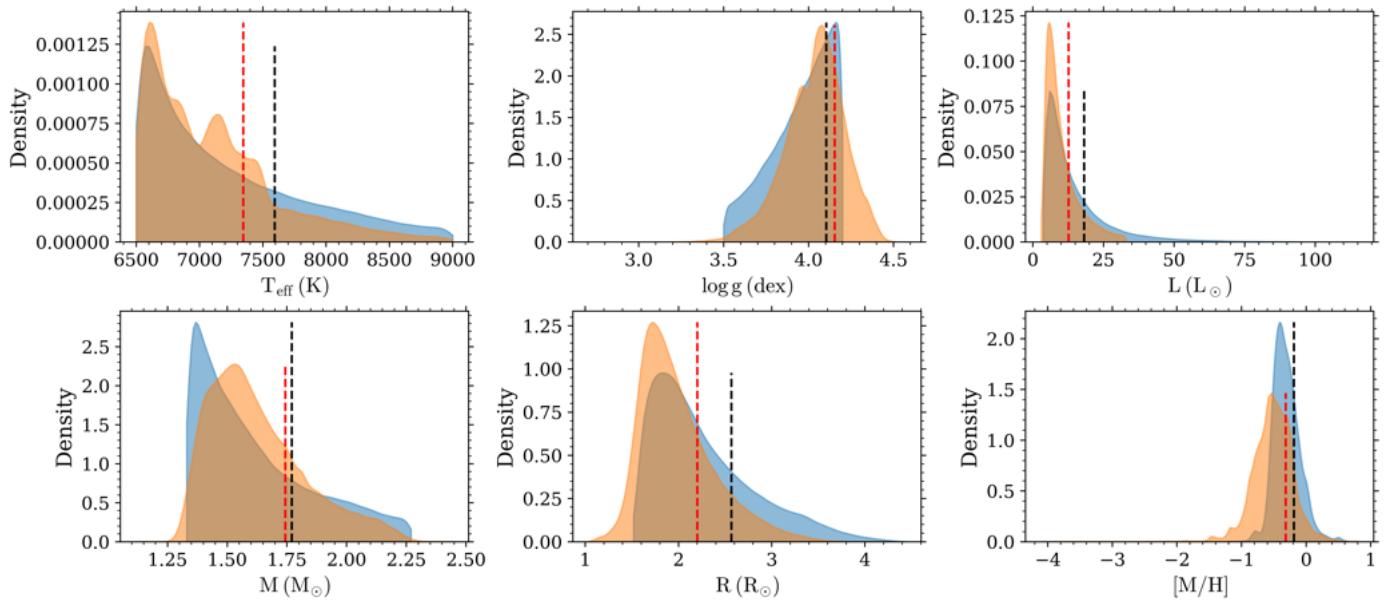

Fig. 2. Gaussian kernel density estimation of the stellar parameters. TESS parameters distributions are plotted in light blue, while Gaia's are orange. The black and red dashed lines indicates 75$^{\text{th}}$ percentile for TESS and Gaia, respectively.

and is therefore only available for sources with $T_{\text{eff}} > 7500$ K. This reduced sample is dominated by rapidly rotating stars with $v \cdot \sin i \in [50, 150]$ km/s, but it also includes a sub-sample of more than 300 slowly rotating stars (or low inclination angle i), as shown in Fig. 3.

4. Stellar variability

4.1. Light curve processing

For each star, a single light curve was constructed by combining the light curves from consecutive sectors. The sectors were stitched together while preserving the inter-sector gaps in order to maintain amplitude and phase coherence. In addition, frequencies below 0.1 c/d were removed using

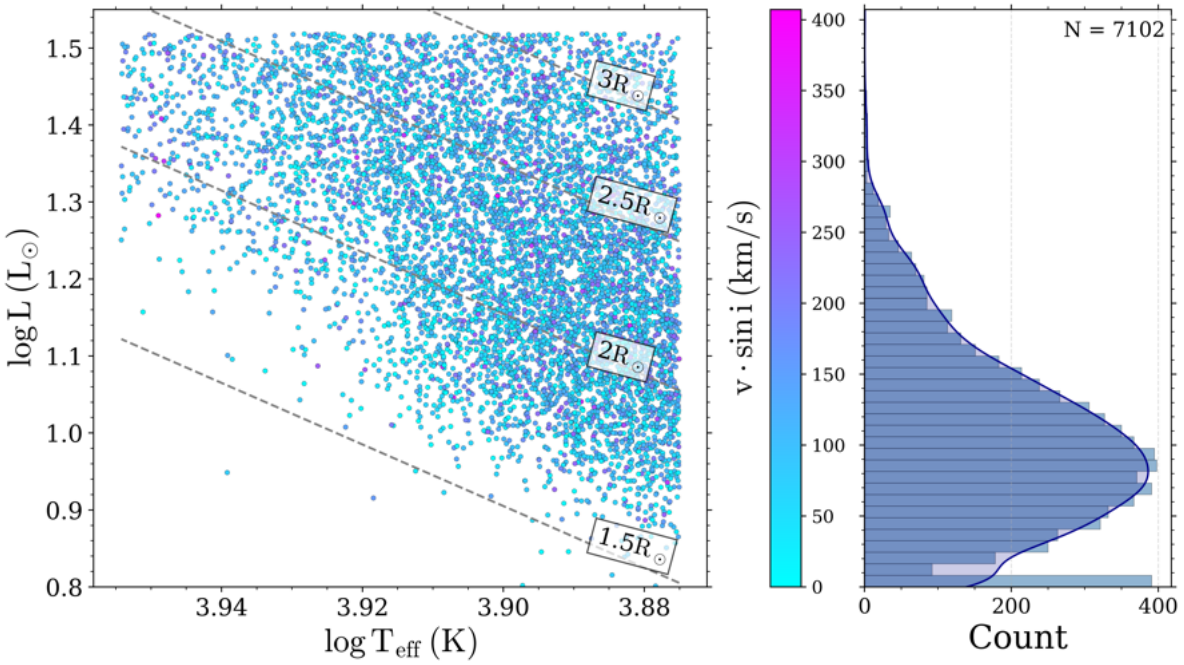

Fig. 3. *Left*: Hertzsprung–Russell diagram of the sample using *ESP-HS* effective temperatures for $T_{eff} > 7500$ K and *FLAME* luminosities, color-coded by projected rotational velocity from Gaia DR3. Dashed lines indicate stellar radii derived from the Stefan–Boltzmann relation. *Right*: Histogram of the same sample projected rotational velocity (50 bins) together with the corresponding kernel density estimate. Y-axis is shared with the colobar from left plot.

a Savitzky-Golay filter (Savitzky & Golay 1964). Owing to the smooth nature of this filter, a window length of 25 days was adopted for each polynomial segment, as the filter begins to attenuate signal power at approximately half the selected timescale.

4.2. Frequency extraction

From the processed multi-sector light curves, the most significant oscillation frequencies in the range $[0, 100]$ c/d were extracted using the code *MultiModes*[7] (Pamos Ortega et al. 2022). *MultiModes* identifies the frequency with the highest amplitude using the Fast Lomb-Scargle periodogram (Press & Rybicki 1989). The light curve is then fitted at that frequency, amplitude, and phase through non-linear optimization of a multi-sinusoidal model, with the parameters refined via a simultaneous fit (in this work, each iteration simultaneously fits the 20 highest-amplitude frequencies). The fitted signal is subsequently removed from the original light curve, and the procedure is iterated on the residuals until the stopping criterion is met (here, S/N = 4.0 following Breger et al. 1990).

The frequency range from 0 to 100 c/d was adopted to optimize the pipeline in terms of computational cost, while ensuring that all pulsation frequencies expected for γ *Dor* and δ Scuti stars were included, albeit at the expense of excluding a substantial fraction of the possible oscillation spectrum of roAp stars. For this reason, when frequencies in the range $[80, 100]$ c/d are detected, the star is flagged as a potential roAp candidate (denoted as R in the catalogue). As shown in Fig. B.1, light curves with cadences of 20s, 120s, and 200s comfortably cover this frequency range, given their Nyquist frequencies of $f_{Ny} = 2160$ c/d, $f_{Ny} = 360$ c/d, and $f_{Ny} = 216$ c/d, respectively. In contrast, for cadences of 600s and 1800s, with $f_{Ny} = 72$ c/d and $f_{Ny} = 24$ c/d, respectively, *MultiModes* may return super-Nyquist frequencies ($f > f_{Ny}$). Given the high regularity of the default TESS sampling (no sampling offset was introduced in this work), it is not possible to identify multiplets out of the Nyquist aliases (Murphy 2015). Consequently, frequencies above the Nyquist limit are discarded in SPATO, as they are highly likely to be aliased representations of sub-Nyquist signals.

Another effect considered during the frequency post-processing is the presence of aliases arising from the convolution with the spectral window function, $W(f)$. As illustrated in Fig. B.2, the window function for stars observed in a single sector exhibits non-negligible sidelobes, with power reaching up to $\sim 30\%$ of the original amplitude (see the case of 200s cadence). These effects are significantly mitigated by adding additional sectors to the light curve, i.e., by extending the total observing time T (see Fig. B.3). Accordingly, the window function is evaluated for each light curve (single or made of multiple sectors) to identify potential alias frequencies. Frequencies that coincided with peaks of the window function and had a contribution greater than 1% ($W(f) \geq 10^{-2}$) were considered suspects of being spurious. Frequencies that resulted from the sum of an observational frequency and a window-function frequency were also considered spurious, provided that the theoretical amplitude of such a combination was at least one tenth of the observed amplitude for that frequency.

[7] Maintained version: `https://github.com/javier-iaa/MultiModes`

Excluding possible aliases and adopting the Rayleigh frequency as the theoretical limit for resolving two close frequencies, we also identify likely harmonics, subharmonics, or linear combinations. We defined harmonics as $|f - nf_i| \leq f_R$ for all $i \in 0, 1, 2, \ldots, 10$, i.e. 10 highest-amplitude frequencies, with n taking integer values between -5 and 5. Subharmonics as $|f - \frac{1}{n} f_i| \leq f_R$, and possible linear combinations among the 10 highest-amplitude independent frequencies of the form $|f - (n_i f_i \pm n_j f_j)| \leq f_R$ for all $i, j \in 0, 1, 2, \ldots, 10$, where f denotes each extracted frequency, (f_i, f_j) are independent frequencies such as $i \neq j$ and (n_i, n_j) are integer coefficients in the range $[-5, 5]$.

The information related to the derived frequencies has been compiled in a separate table from the main catalogue, with the columns described in Table A.4.

4.3. Classification of stars

For the classification of the stars in SPATO, only those frequencies that satisfy three requirements are considered: they are unlikely to be spurious due to the window function, they have an S/N greater than 5.0, and they are independent, meaning that they are neither harmonics, subharmonics, nor linear combinations of independent frequencies, as defined in Sect. 4.2.

Table 3. Frequency ranges adopted for the classification of pulsating stars based on their independent frequencies.

Pulsator	Range (c/d)	Description
Generic variability	0–0.5	Binaries, rotational modulation, etc.
γ Dor	0.5–5.0	
δ Scuti	5.0–80.0	
roAp	> 80	roAp candidates

The frequency spectrum was divided into four well-defined regions, as summarized in Table 3. Based on the location of the independent frequencies within these regimes, several categories were defined:

- **Constant stars**: No oscillation frequencies were detected in any regime (tagged as "C" in the catalogue).
- **Pure pulsators**: All independent frequencies lie within a single pulsation regime ("D" for δ Scuti, "G" for γ Doradus, and "R" for roAp). To avoid misclassifying rotationally-modulated or elliptic stars as γ Dor, we require at least 2 independent frequencies.
- **Hybrid pulsators**: Independent frequencies are present in two or more pulsation regimes (e.g., "DG", "GD", etc.).
- **Other variability**: If a star that is classified as pure, or hybrid shows at least one independent frequency within the generic-variability region in addition to one or more pulsation regimes, the star is classified as pure, or hybrid accordingly, and flagged as exhibiting additional variability of a different nature (the flag "OTHER" is set to 1 in the catalogue). If all independent frequencies fall in the generic-variability region, then star is catalogued as variable but not pulsating ("N" in this paper).

To establish the main pulsation type in hybrid pulsators, i.e., to classify whether a hybrid belongs to the "GD" or "DG" category, we define a new statistical parameter: the dominant pulsation frequency. Since the amplitude traces the energy carried by a pulsation mode, this parameter identifies the pulsation regime containing most of the spectral energy. Firstly, an amplitude-weighted cumulative distribution of the independent frequencies is computed. Specifically, the amplitude of each independent frequency is weighted by the sum of all amplitudes:

$$w = \frac{A}{\sum_i A_i}$$

where A is the amplitude (in parts per million) of a given independent frequency, and $\sum_i A_i$ is the total amplitude summed over all independent frequencies. The dominant pulsation frequency is defined as the frequency f_k at which 60% of the total weighted amplitude is accumulated.

$$\sum_{i}^{i=k} w_k = 0.6$$

The primary pulsator type, whose abbreviation goes first in the hybrid classification name[8], is defined by the regime containing the dominant pulsation frequency.

If independent frequencies are present in three different pulsation regimes, the dominant pulsation frequency is applied to determine the primary type. The secondary type is then assigned to the regime (excluding the primary) containing the largest number of independent frequencies. The third regime is disregarded, as it is highly likely to result from spurious detections or unreliable measurements; such cases are flagged as ambiguous (AMB=1 in the catalogue).

4.4. Variability analysis

From this subsection, we consider only stars present in both the TESS and Gaia queries, i.e. the enriched sample. In addition, the stars shown here have light curves either with cadences $\leq$ 600 s, or 30 min provided that at least three consecutive sectors are available. This restriction enables a more robust classification of δ Scuti, γ Dor, and potential roAp stars, as both p and g modes can be detected below the Nyquist frequency, while extending the time baseline increases the likelihood of detecting lower-amplitude g modes.

The resulting histogram of this selection is presented in Fig. 4. A clear dominance of γ Dor stars and constant stars is observed in the sample relative to other star types. It is likely that, among the stars classified as γ Dor, a significant fraction are outliers affected by binarity or rotational variability, which overlap in the same frequency range. A stricter classification criterion would therefore be desirable, for instance the detection of period spacings, whose presence in γ Dor stars has been reported for hundreds of objects (Li et al. 2019). Alternatively, some of these objects may correspond to nearby evolutionary stages in the Hertzsprung-Russell diagram, such as highly evolved solar-like stars with incorrectly determined stellar parameters, or RR Lyrae variables. However, a detailed assessment, requiring an analysis of the frequency spectrum up to the Nyquist limit (i.e., beyond 100 c/d) and a careful revision

[8] For the "DG" case, δ Scuti would be the primary pulsator type

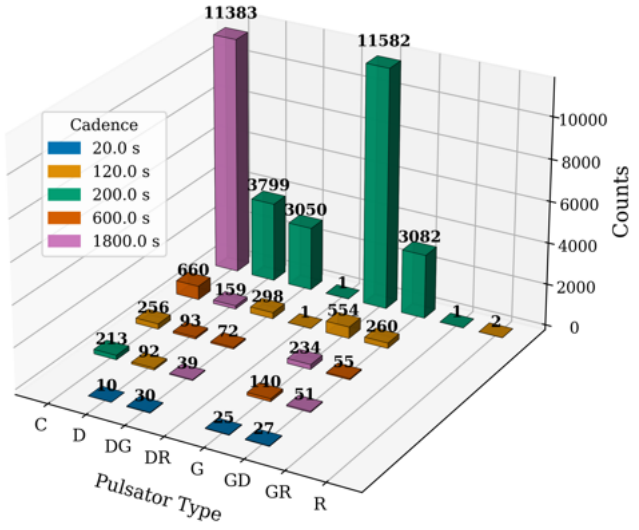

Fig. 4. Histogram of pulsating stars grouped by the cadence of their light curves, where "D" denotes δ Scuti, "G" γ Doradus, "R" roAp, a two-letter combination "XY" indicates a hybrid pulsator with primary type "X", and "C" constant stars.

of the adopted photometric apertures to identify potential contaminants is beyond the scope of this work. These objects are labeled as candidate γ Dor stars pending further analysis.

Regarding the constant stars, the majority correspond to objects observed in long cadence (30 min), which prevents adequate sampling of high-frequency variability and potential p modes that could modify these statistics. It should also be noted that the frequency extraction with *MultiModes* is limited to 100 c/d (see Section 4.2), and that outliers may be present even among for stars with cadences of 20s, 120s, or 200s. This effect was partially mitigated through prior selection of stellar parameters (see Section 2).

The complete statistics, i.e., the distribution of pulsators in TESS regardless of the availability of Gaia parameters, are shown in Fig. B.4. The large numbers highlight the significant potential of the catalogue and the wide range of studies enabled by the availability of oscillation frequencies for these stars.

A comparable number of "pure" and hybrid δ Scuti stars are detected, with a total of 7,675 objects that will be used in the subsequent analyses of this work. This number is also similar to that of the hybrid γ Dor - δ Scuti stars, but significantly larger than the number of stars with roAp oscillations, with 5 objects. Among these 5, we catalogued 2 pure roAp: TIC 376942777 (classified in literature as roAp; Balona 2022) and TIC 255756402 (new); 2 hybrids δ Scuti - roAp: TIC 260266413 (new hybrid) and TIC 260654645 (classified in literature as HADS; Antoci et al. 2019); 1 hybrid γ Dor - roAp: TIC 231972884 (new). We expect the latter to be a pure roAp with stellar spots, thus γ Dor frequencies may be due to rotation periods (Holdsworth et al. 2024).

For comparison and validation, the VSX catalogue identifies 7,512 stars in this sample under the category "DSCT|GDOR|SXPHE" (δ Scuti, γ Dor, or SX Phoenicis). We obtain an agreement rate of 64% for this category, which increases to 74% when excluding stars with 30 min cadence light curves. This same 74% agreement is also found when considering the full SPATO catalogue with respect to VSX.

The remaining VSX classifications present in the sample (eclipsing binaries, Cepheids, RR Lyrae, etc.) amount to 675 objects (less than 10% of the "DSCT|GDOR|SXPHE" category). In our catalogue, these stars are classified either as constant[9], as generic variables, or in a few cases as δ Scuti/γ Dor/hybrid pulsators. Therefore, overall, the classification presented in this work shows a good level of consistency with VSX, while reflecting the different methodological criteria and observational constraints adopted here.

Using the detected and classified variability, and cross-matching with the catalogue of Hunt & Reffert (2024), we identified open clusters hosting δ Scuti stars, whether pure or hybrid. Table 4 lists the seven open clusters containing at least five δ Scuti stars. With the new PLATO data, these clusters can provide deeper insight into δ Scuti pulsations, as they consist of stars of the same stellar population, since they arise from the same molecular cloud. In particular, NGC 2477 is especially interesting in light of recent studies (Palakkatharappil & Creevey 2023) and the presence not only of δ Scuti stars, but also of blue and yellow stragglers (Rain et al. 2020).

Stars classified as pure δ Scuti, pure γ Dor, or their respective hybrids were placed in an HR diagram using Gaia parameters (see Fig. 5).

Despite differences in number density, all types are essentially distributed within the same region of the HR diagram. This effect is particularly evident for the pure γ Dor stars. A significant fraction is located below the red edge of the γ Dor theoretical instability strip (GIS), while numerous objects are also found above the theoretical blue edge, encroaching into the typical δ Scuti domain. This fact reinforces the possibility of γ Dor stars misclassification, potentially representing other types of variability. Nevertheless, a tendency toward slightly higher effective temperatures is apparent for the hybrid γ Dor - δ Scuti stars. Most of them cluster in the intermediate region between both pulsator types, although some objects are located close to the blue edge of the δ Scuti classical instability strip.

For the δ Scuti stars, both pure and hybrid, the majority lie within classical instability strip (IS), as expected. However, in both cases a subset of objects is found below the red edge. Pure δ Scuti stars do not show an uniform distribution along the IS; instead, a higher concentration toward the red edge is observed. No clearly dominant evolutionary

Table 4. Open clusters hosting δ Scuti stars, either pure or hybrid, within the LOPS2 field observable by PLATO.

Open cluster	Number of δ Scuti stars
NGC 2477	99
UBC 1455	10
NGC 2354	8
NGC 2516	7
Ruprecht 27	6
Alessi 3	5
FSR 1284	5

[9] Either because they pulsate beyond 100 c/d or because they have 30 min cadence light curves

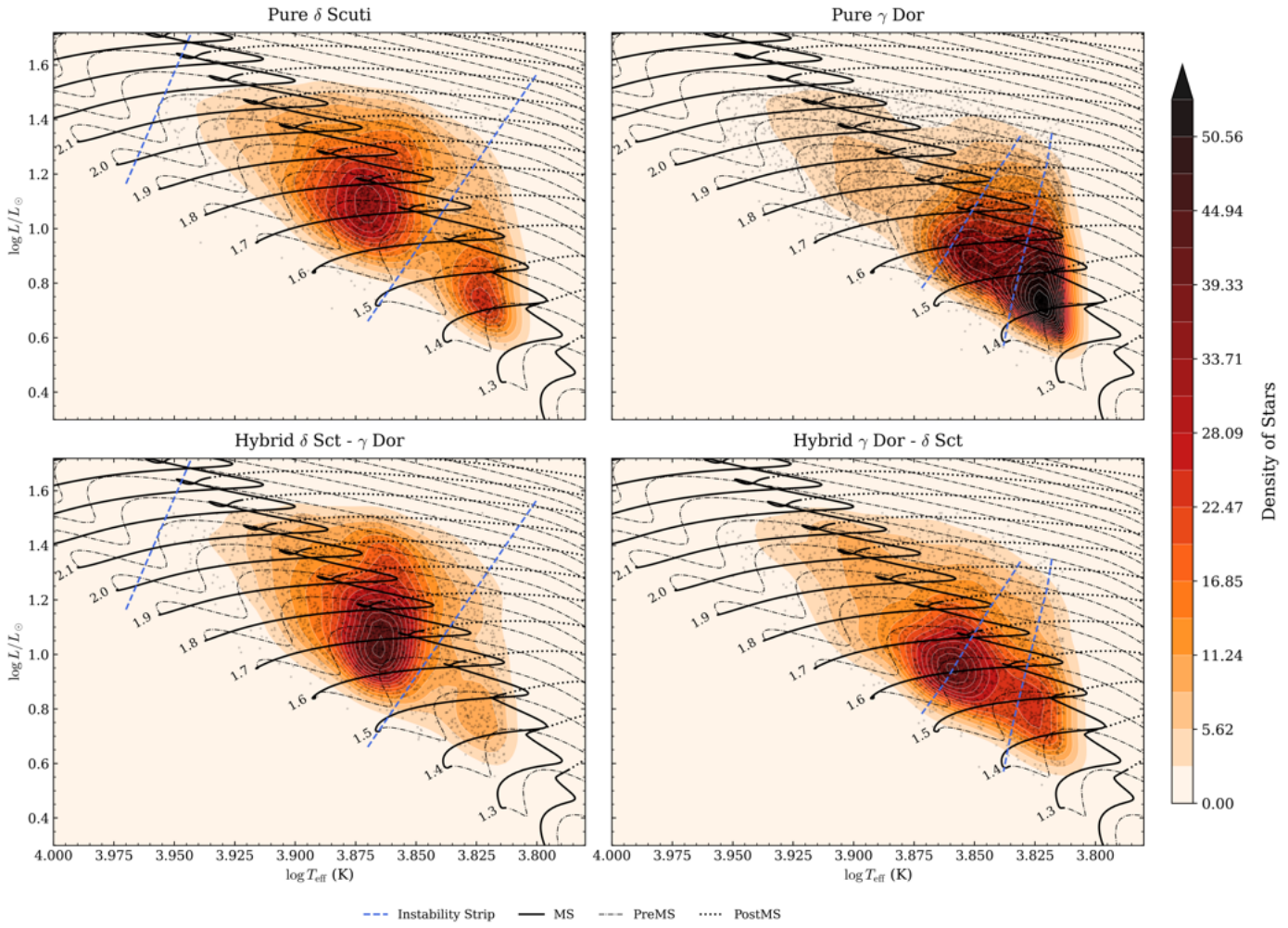

Fig. 5. HR diagrams with Gaia parameters of stars with light curve cadences below 1800s, or with at least 3 sectors if 1800s cadence. *Left*: Pure (top) and hybrids (bottom) δ Scuti that fell in TESS and Gaia query location in the HR diagram with the classical instability strip region delimited by a dashed line from Murphy et al. (2019). *Right*: Pure (top) and hybrids (bottom) γ Dor both in TESS and Gaia queries with the theoretical instability strip region delimited by a dashed line from Dupret et al. (2005).

stage is identified, as the stars are not preferentially distributed either along the ZAMS or toward the TAMS. In contrast, the hybrids appear to exhibit a somewhat narrower temperature range.

Overall, a classification based solely on the detectability of absolute frequency ranges, as adopted in this work, does not yield a clear structural or evolutionary separation, given the strong overlap observed among all pulsator types in this region of the HR diagram.

In terms of pulsator fraction, a low value is observed across the IS, with a maximum of 38.0% at 7562 K. This value is just about half of that reported by Murphy et al. (2019), who found a fraction of approximately 60% within the IS. The discrepancy arises from the different classification criteria adopted. In this work, stars are classified as δ Scuti only when the majority of the spectral energy is concentrated in the 5–80 c/d range. In contrast, Murphy et al. (2019) classified a star as δ Scuti if at least one independent p mode above 5 c/d was detected with sufficient S/N to yield a positive amplitude skewness.

To make both criteria comparable, we broaden our definition to include also hybrid γ Dor - δ Scuti stars since they show p modes above 5 c/d. The peak pulsator fraction then increases to 47.0% at 7,562 K, as shown in Fig. 6. Although this value does not reach that reported by Murphy et al. (2019), it becomes comparable, and the remaining differ-

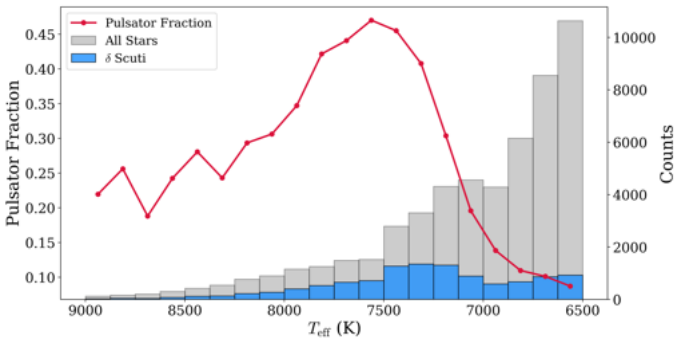

Fig. 6. δ Scuti pulsator fraction on the left y-axis and number counts on the right y-axis, as a function of effective temperature on the x-axis. The red line represents the ratio between the stars classified as δ Scuti in this section and the total number of stars in that bin.

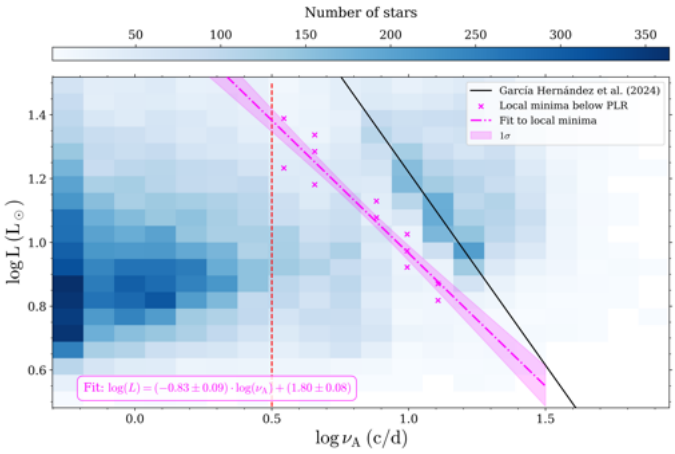

Fig. 7. Luminosity as a function of the frequency ν_A, i.e. the independent frequency above 0.5 c/d with the highest amplitude. The solid black line represents the Period–Luminosity relation derived by García Hernández et al. (2024). The red dashed line indicates the frequency limit at 5 c/d. Magenta dashed-dotted line represents the best fit of the gap between the PLR and 5 c/d with its uncertainty as a filled magenta band. The stars shown here are classified as δ Scuti, or γ Dor, or hybrid pulsators (both δ Scuti-γ Doror γ Dor-δ Scuti).

ences may be attributed to the large number of stars observed with 30 min cadence. This distinction, along with the structural undifferentiation shown in Fig. 5, highlight the need for well-established observational constraints to classify δ Scuti, γ Dor and hybrids. An empirical or observational criterion is needed to define these pulsators in physical terms and it would enrich approaches to disentangle the systematic non-/coexistence of two excitation mechanisms in AF-type stars along the main sequence and early post-MS phases: the opacity (κ) mechanism operating in the He II ionization zone (Breger & Montgomery 2000) and convective blocking (Dupret et al. 2005; Guzik et al. 2000).

5. The Period-Luminosity diagram

5.1. δ Scuti and γ Dor separation

Our catalogue, SPATO, offers a critical look at a large, homogeneous population of stars with their available oscillation frequencies. This allows for a deeper exploration of the observational distinction of a δ Scuti, a γ Dor, or a hybrid pulsator. Taking advantage of the fact that δ Scuti stars occupy a well-defined region in the Period-Luminosity Diagram (PLD; McNamara 2011; Martínez-Vázquez et al. 2022; Ziaali et al. 2019), we investigate the PLD of the stars in order to identify well-separated clusters that may allow us to distinguish between these types of pulsators (see Fig. 7). The frequency (equivalent to the period) was determined as the independent frequency ν_A with the highest amplitude and satisfying ≥ 0.5 c/d, in order to remove possible frequencies caused by instrumental effects or other types of variability.

Two regions with a higher density of points can be distinguished from the whole sample, i.e. 27,165 objects. The first lies along the Period-Luminosity Relation (PLR) proposed by García Hernández et al. (2024) and slightly above it, while the second is located toward the lower-left edge of the diagram. Indeed, the 5 c/d limit acts as a rough separator between both groups. However, a more precise delimiter can be obtained by tracing the local valley between the PLR and the 5 c/d boundary (Eq. 1). This valley is the best-fit line to the centers of the bins with the lowest number of counts between 5 c/d and the PLR of García Hernández et al. (2024)

$$\log(L) = (-0.83 \pm 0.09) \cdot \log(\nu_A) + (1.80 \pm 0.08) \quad (1)$$

We propose that this valley may serve as a potential, purely observational discriminator between δ Scuti and γ Dor stars. Thus, pulsating A-type stars within the IS located above Eq. 1 would be classified as δ Scuti, while those below it would be classified as γ Dor. Using the classical classification based on the 5 c/d threshold, 10.95% of the hybrid δ Scuti-γ Dor stars exhibit $\nu_A \leq 5$ c/d, while 6.49% of the γ Dor-δ Scuti hybrids show $\nu_A \geq 5$ c/d. In other words, these hybrids have their highest-amplitude frequency in the pulsation regime that contains less total energy, which makes them particularly interesting in terms of excitation mode selection.

5.2. Theoretical Q values of δ Scuti

We used a grid of models to compute the theoretical pulsation constant Q of stars classified as δ Scuti stars. To that end, we have retrieved the grid of rotating models presented in Rodríguez-Martín et al. (2020). This grid contains almost half a million stellar equilibrium and oscillation models representative of intermediate-mass stars (i.e., masses between M = [1.3, 3.0] $M_\odot$). The equilibrium models were computed with the code CESTAM (Marques et al. 2013), covering from the early pre-main sequence (where the protostar is coupled with its protoplanetary disk) up to the sub-giant branch. We varied the mass (in steps of 0.05 $M_\odot$), the metallicity ([Fe/H] = [-0.4,0.2] dex in steps of 0.1) and the initial rotation velocity. The latter is obtained by varying the initial rotation period of the protostar (0, 5, 6 and 7 days) and the time (τ) during which the star and the protoplanetary disk are locked (fixed to 5 days). The mixing length parameter was fixed to $\alpha = 1.64$ without overshoot. Rotationally induced mixing was taken into account after Zahn (1992) and a further refinement by Mathis & Zahn (2004) for the radiative zones of the stellar interior (more details in Marques et al. 2013). The stellar models were computed to rotate with $\Omega/\Omega_C \lesssim 0.7$, the vast majority below 0.5, being Ω_C the critical rotational velocity, in which the centrifugal forces surpass the gravitational ones.

Stellar adiabatic oscillations were computed using the FILOU code (Suárez & Goupil 2008). It computes adiabatic oscillations using a perturbative approximation up to the second order and takes into account the stellar distortion on the frequencies due to centrifugal forces. Additionally, the code includes the calculation of near-degeneracy effects (see Suárez et al. 2006, for more details). Modes with spherical degrees $0 \leq \ell \leq 2$ were computed for each equilibrium model, from a few low-order g modes up to the cut-off in p modes.

The Q values were obtained for the radial modes ($\ell = 0$) with $n = [1, 8]$ using the stellar mean density (Breger et al. 1990):

Table 5. Theoretical Q values.

Constant	Range (d)	F0/Fn
Q1	[0.03070, 0.03440]	–
Q2	[0.02440, 0.02716]	[0.7391, 0.8491]
Q3	[0.01978, 0.02233]	[0.5851, 0.7071]
Q4	[0.01647, 0.01899]	[0.4760, 0.5942]
Q5	[0.01418, 0.01635]	[0.4015, 0.5181]
Q6	[0.01242, 0.01430]	[0.3466, 0.4565]
Q7	[0.01100, 0.01270]	[0.3039, 0.4067]
Q8	[0.00984, 0.01140]	[0.2697, 0.3650]

$$Q = P\sqrt{\bar{\rho}/\bar{\rho}_{\odot}} \tag{2}$$

Special caution has been taken when computing the mean density of a rotating star. We have accounted for stellar oblateness using a Roche model to calculate the volume and then the mean density. Additionally, we restricted our calculations to models located in the observational instability strip of δ Scuti with boundaries taken from Murphy et al. (2019). The results are shown in Table 5. Some ranges are found for each radial orden, since Q can slightly vary with stellar rotation and metallicity (Suárez et al. 2006), but radial orders up to $n = 4$ do not overlap.

5.3. Observational Q values of δ Scuti

The stellar parameters L, $\log g$, and $T_{\rm eff}$ estimated by Gaia DR3 can be used to compute the pulsation constant Q (Breger et al. 1990):

$$\log\left(\frac{Q}{P}\right) = -0.25\log\left(\frac{L}{L_{\odot}}\right) + 0.5\log\left(\frac{g}{g_{\odot}}\right) + \log\left(\frac{T_{\rm eff}}{T_{\rm eff\odot}}\right) \tag{3}$$

This allows a preliminary inspection of the distribution of the dominant pulsation modes linked to $\nu_{\rm A}$ represented in the PLD. Naturally, this estimate depends strongly on stellar parameters that may carry significant uncertainties. However, given the large sample size in this work, we assume that the statistical trends remain robust despite these uncertainties.

The left panel of Fig. 8 shows the distribution of Q values along the PLD. For the purpose of mode identification, we adopt the reference values listed in Table 5, computed as described in Sect. 5.2. In this table, the fundamental radial mode and several overtones show well-separated ranges in Q, whereas higher orders start to mix. This separation between overtones allows a fair estimation of the position of radial modes up to n = 4.

On the other hand, the right panel of Fig. 8 illustrates the distribution of $\log Q$ for each pulsator type classified in this work as a function of the horizontal distance to the PLR. A strong overlap is evident when using the classical selection criterion.

The combined visualization of the left and right panels allows us to identify, within the PLD, the type of pulsator (δ Scuti pure, hybrids, and γ Dor) location along the PLR and the pulsation mode which is exciting the most, according to the classification in Table 5. From this global view, we find that PLR is mostly populated by pure δ Scuti stars, hybrid δ Scuti-γ Dor stars, and γ Dor-δ Scuti stars whose frequencies ν_A corresponds to the radial fundamental. We also find that higher overtones occupy regions above it, such that the higher the overtone, the farther it is located above the PLR.

The group of γ Dor-δ Scuti stars located above the PLR (positive X-axis in right panel of Fig. 8) is particularly noteworthy. They are stars whose spectral energy distribution is dominated by low frequencies, yet whose dominant frequency $\nu_{\rm A}$ lies in the δ Scuti regime and corresponds to the radial fundamental mode or one of its overtones. The opposite situation is also observed: hybrid δ Scuti-γ Dor stars with a dominant frequency in the g-mode regime but with an overall energy distribution favoring p modes. A detailed analysis of this behavior could provide insight into mode selection mechanisms. In particular, it is worth exploring whether this could be a signature of possible High Amplitude δ Scuti stars (HADS) behavior in the context of γ Dor-δ Scuti stars located above the PLR.

The distribution of the different pulsation modes for stars with any δ Scuti pulsations (called simply δ Scuti from now on) is plotted in Fig. 9. Differences are observed in the distribution of excited modes compared with the results of Poro et al. (2024). In their work, the radial fundamental mode and the first overtone are found to be the most frequent, and a larger number of stars excite the third overtone compared to the second. We find as well a higher number of δ Scuti exciting the third overtone over the second, but we find similar preference for exciting the third overtone, the first overtone, or the radial fundamental mode. This discrepancy is due to a large number of stars exhibiting Q values between those expected for the radial fundamental mode and the first overtone. This may indicate uncertainties in the stellar parameters used to compute Q. Another possible explanation, as suggested by García Hernández et al. (2024), is that the effects of rapid rotation, common among A-type stars, have not been taken into account. Rotation, and consequently gravity darkening, can make measurements of luminosity, $\log g$, and $T_{\rm eff}$ highly dependent on the inclination angle i. This would broaden the distribution around the PLR, leading to systematic underestimation or overestimation of these parameters. Despite this, these results open the possibility of constructing a high-quality sample to investigate excitation mechanism selection in δ Scuti stars.

On the other hand, a large number of stars exhibit Q values between those expected for the radial fundamental mode and the first overtone. This may indicate uncertainties in the stellar parameters used to compute Q. Another possible explanation, as suggested by García Hernández et al. (2024), is that the effects of rapid rotation, common among A-type stars, have not been taken into account. Rotation, and consequently gravity darkening, can make measurements of luminosity, $\log g$, and $T_{\rm eff}$ highly dependent on the inclination angle i. This would broaden the distribution around the PLR, leading to systematic underestimation or overestimation of these parameters.

Another interesting feature visible in the left panel of Fig. 8 is that each pulsation mode seems to follow its own linear relation with luminosity. In Fig. 10 we present the dependence of ν_A on luminosity for each pulsation mode. This linear behavior was already noted by Poro et al. (2024) but

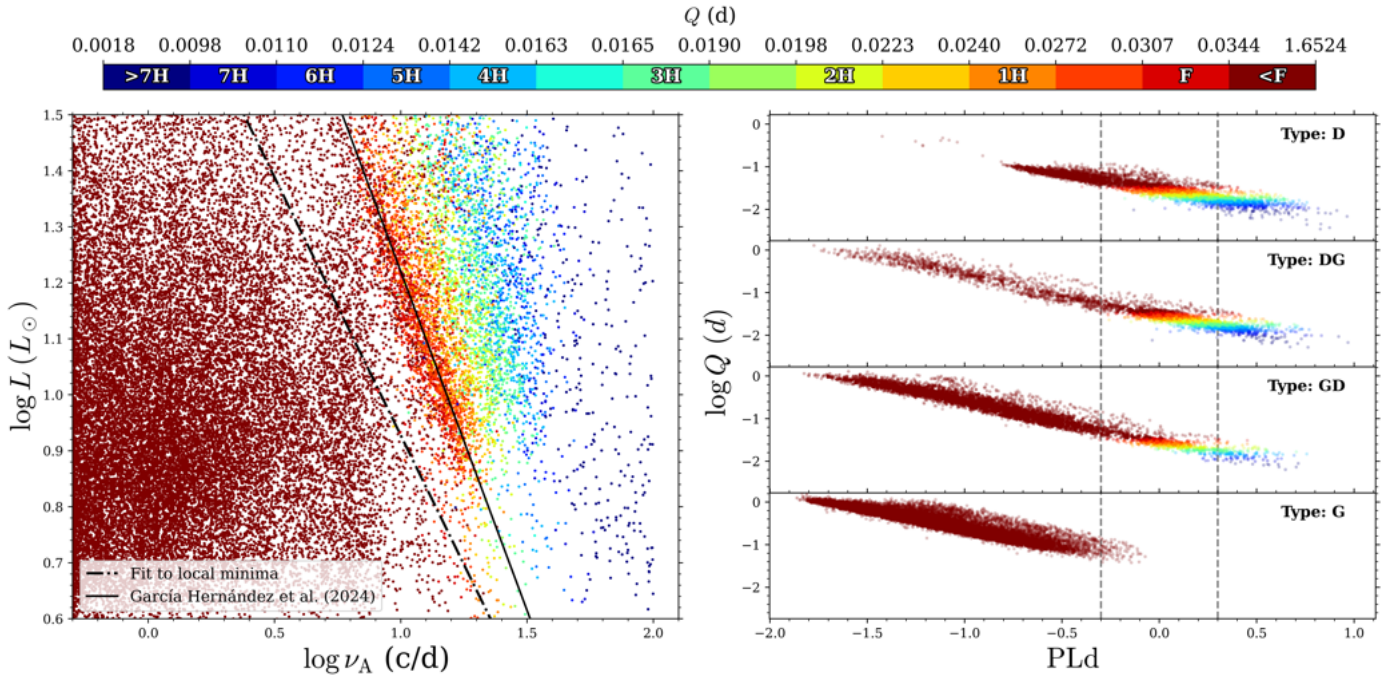

Fig. 8. *left*: Luminosity as a function of the frequency $\nu_{\rm A}$, i.e. the independent frequency above 0.5 c/d with the highest amplitude. The solid black line represents the Period–Luminosity relation derived by García Hernández et al. 2024 while dashed-dotted line corresponds to Eq. 1. *right*: Distance of the points to the PLR versus $\log Q$ computed from equation 3. Dashed line is at an absolute distance 0.3 from PLR. *Both*: Q is color coded, with F as the fundamental radial mode and XH the $\rm X^{th}$ overtone.

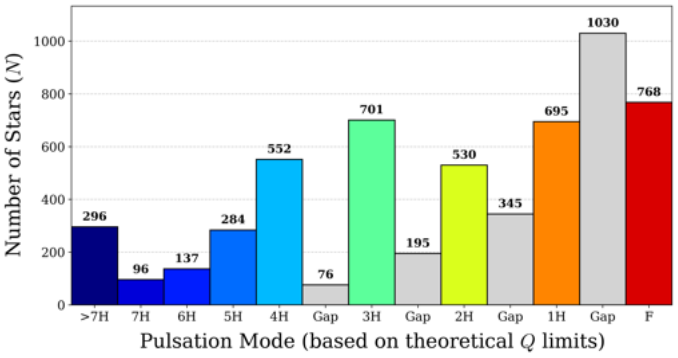

Fig. 9. Histogram of Q along δ Scuti stars, either pure or hybrids of any dominant pulsator. Gaps are plotted in grey and $Q < F$ is omitted.

for the absolute magnitude in the V band and the period up to the third overtone.

In this work, we also find linear relations between the frequency ν_A of the radial fundamental mode and the first overtone with luminosity, in our case they are nearly parallel. The frequency separation between these two relations, assuming they are parallel, i.e. adopting the mean of their slopes ≈ -1.065:

$$1\mathrm{H}: \ \log L \approx -1.065 \log \nu_{1\mathrm{H}} + 2.38 \quad (4)$$

$$F: \ \log L \approx -1.065 \log \nu_{F} + 2.25 \quad (5)$$

$$1\mathrm{H} - F: \ \frac{\nu_F}{\nu_{1\mathrm{H}}} \approx 0.76 \quad (6)$$

This value is in agreement with literature (Stellingwerf et al. 1979) and supports the mode identification performed based in Q values.

For higher overtones the slope becomes progressively shallower and the dispersion increases, which may be due to the presence of non-radial modes contaminating the sample. The relation found for the fundamental radial mode is consistent with the short-period regime reported by Martínez-Vázquez et al. (2022). However, δ Scuti stars with ν_A in the second overtone or higher, most likely correspond to non-radial modes and tend to be concentrated in regions of higher luminosity compared to radial or first-overtone pulsators. The color of the points represented as the value of $\mathrm{v} \cdot \sin \mathrm{i}$ shows no clear dependence between the projected rotational velocity and the position of the stars in the Period-Luminosity relation, suggesting that projected rotation does not introduce a dominant bias in the derived relation. It is also true, nevertheless that it may contribute to the observed dispersion and determining the equator velocity may help to clarify this dispersion.

6. Estimating R and $\log g$ from ν_A

The period (or equivalently the frequency) of radial modes is related to the mean stellar density through the pulsation constant Q (see Eq. 2). Therefore, the period of these pulsation modes is also linked to the stellar radius R and mass M. While the mass is typically affected by large uncertainties, a more direct observational proxy is the surface gravity, $\log g = \log(G \cdot M/R^2)$.

It is thus expected that the frequency ν_A of these radial modes can act as an estimator of both R and $\log g$. This is explored in Fig. 11, using radii estimated from *FLAME* and $\log g$ values from *GSP-Phot*.

For the radial fundamental mode and the first overtone, we find a strong (R>0.86) and well-separated linear relation of $\log \nu_A$ with both $\log R$ and $\log g$. Higher overtones are

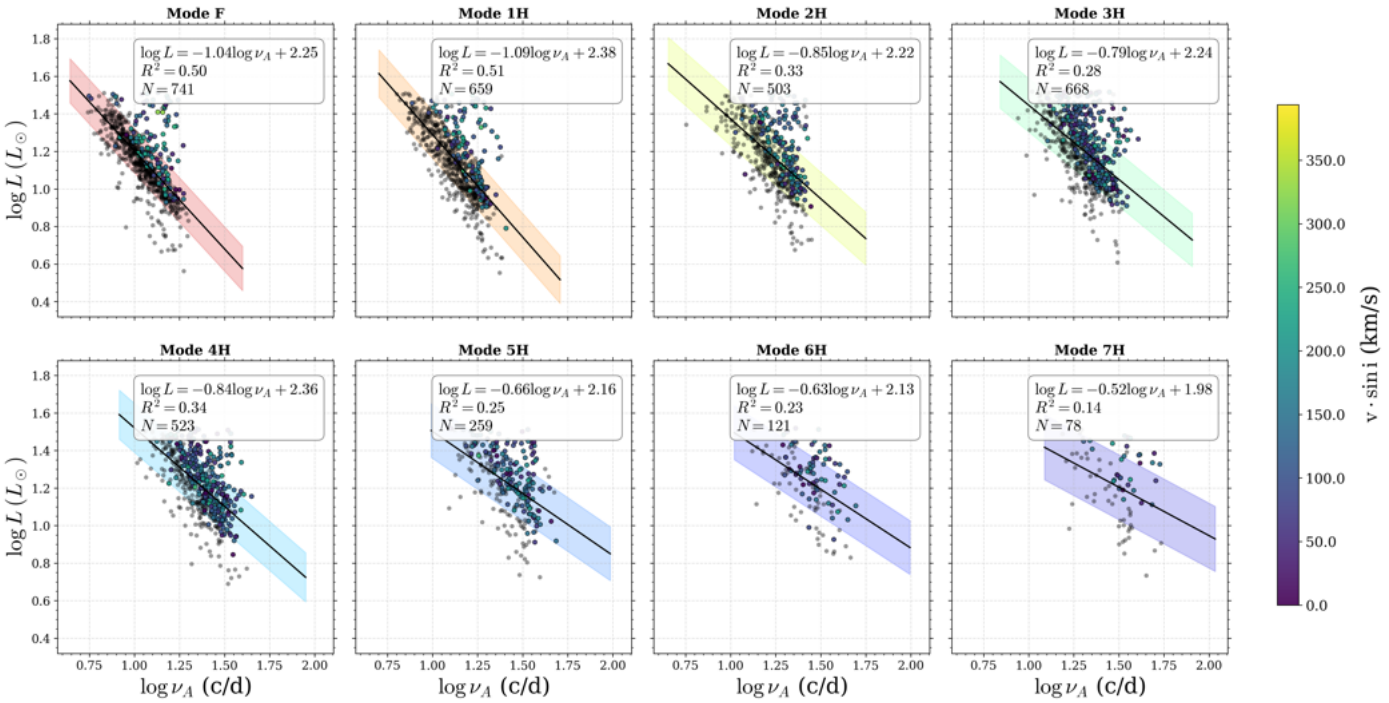

Fig. 10. Luminosity as a function of the frequency ν_A, separated according to the overtone to which it belongs as determined from Q. All stars shown here are δ Scuti or hybrid pulsators of any dominance.

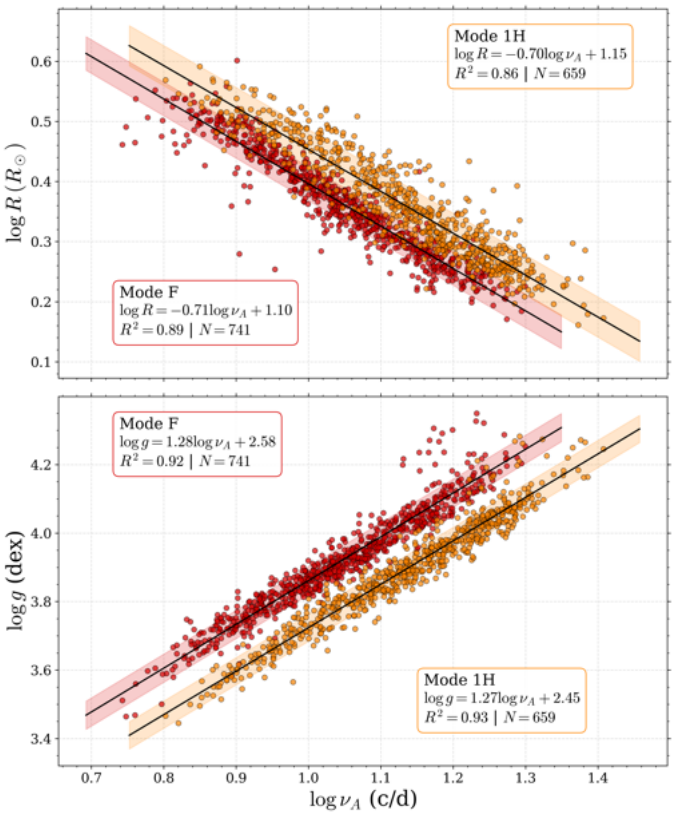

Fig. 11. $\log \nu_A$ from TESS light curves versus $\log R\,(R_\odot)$ (*top*) and $\log g$ (*bottom*) from Gaia data. The fundamental radial mode (red) and the first overtone (orange) are highlighted, together with the derived scaling relation and its uncertainty.

not considered in this analysis, as the increasing dispersion seen in Fig. 10 suggests that many of these modes are likely non-radial, as discussed above.

The relations shown in Fig. 11 combine three independent sources of information. First, the expected Q ranges are taken from the theoretical models described in Sect. 5.2. Second, the observational Q values are derived from Gaia DR3 stellar parameters. Third, the associated frequencies are measured directly from TESS light curves. The tight dependence of $\log \nu_A$ on $\log R$ and $\log g$, based on these independent inputs, provides strong support for identifying stars pulsating at ν_A as either radial fundamental mode F (red) or first overtone 1H (orange).

If confirmed, such a strong observational constraint would reduce the uncertainties in these physical parameters and improve the agreement with theoretical stellar models. In addition, it could serve as a valuable diagnostic for $\log g$ determinations from spectroscopy, which are often affected by degeneracies with $T_{\rm eff}$ due to the sensitivity of Balmer lines to both parameters, especially in hot stars with $T_{\rm eff} \geq 8000$ K (Niemczura et al. 2014).

7. Conclusion

We present the SPATO catalogue (S-urvey of P-LATO A-Type stars O-scillation frequencies), which aims to serve as reference for A-Type stars located in the first observation field of the PLATO missino. It includes stellar parameters from TESS and Gaia, together with oscillation frequencies derived from TESS light curves and linear combination analysis. A rigorous classification based on classical criteria (5 c/d boundary) has been performed to separate δ Scuti, γ Dor, hybrid pulsators, constant stars, and roAp stars according to their independent modes distributions.

No clear separation between δ Scuti and γ Dor stars is found in the HR diagram using this standard classification criterion. Instead, a luminosity–dominant mode ν_A

relation is proposed as a purely observational indicator to distinguish between these two pulsator subgroups.

The pulsator fraction within the instability strip, about 47%, is consistent with values reported in the literature, albeit slightly lower, most probably due to the limited spectral domain of many light curves with 30 min cadence.

Mode identification of radial orders has been carried out using values of the pulsation constant, Q. A predominance of radial pulsators in the radial fundamental mode is found along the PLR and in the regions immediately above it, the latter corresponding to higher overtones whose order increases with distance from the PLR. The results appear to support this mode identification at least up to the first overtone, for which we systematically find that $\frac{P_{1H}}{P_F} \approx 0.76$. For the rest of overtones, we suggest they might be mixed with non-radial modes of high degree ℓ. Therefore, from δ Scuti pulsators along the PLR, radius and $\log g$ can be inferred from their $\log \nu_A$ as shown in fig 11, which can be a useful estimator for spectroscopy degeneracy problems related with $\log g$.

These results highlight: the need for more shorter cadence photometric data, complementary approaches from spectroscopy to better constrain stellar parameters, as well as theoretical modeling for mode identification and characterization of the stellar interior and excitation mechanisms selection. But, they also highlight the potential of statistical analysis to understand the pulsation behaviour of A-Type stars and the benefits of catalogues that provide the full information of the pulsation content.

8. Acknowledgements

CCCM acknowledges this paper is part of the grant PID2023-149439NB-C43, funded by MCIU/AEI/10.13039/501100011033 and by the ESF+. AGH and JCS acknowledge support from the project PID2023-149439NB-C43 funded by MICIU/AEI/10.13039/501100011033 and by FEDER, UE. GMM acknowledges financial support from Junta de Andalucía through the program Emergia (EMEC_2023_00533).

This work has made use of data from the European Space Agency (ESA) mission *Gaia*[10], processed by the *Gaia* Data Processing and Analysis Consortium (DPAC[11]). Funding for the DPAC has been provided by national institutions, in particular the institutions participating in the *Gaia* Multilateral Agreement.

This research has made use of the International Variable Star Index (VSX) database, operated at AAVSO, Cambridge, Massachusetts, USA.

This paper includes data collected with the TESS mission, obtained from the MAST data archive at the Space Telescope Science Institute (STScI). Funding for the TESS mission is provided by the NASA Explorer Program. STScI is operated by the Association of Universities for Research in Astronomy, Inc., under NASA contract NAS 5-26555.

References

Aerts, C., Christensen-Dalsgaard, J., & Kurtz, D. W. 2010, Asteroseismology (Springer Netherlands), 1–872
Andrae, R., Fouesneau, M., Sordo, R., et al. 2023, Astronomy and Astrophysics, 674, A27
Antoci, V., Cunha, M. S., Bowman, D. M., et al. 2019, MNRAS, 490, 4040
Baglin, A., Auvergne, M., Barge, P., et al. 2006, ESASP, 1306, 33
Balona, L. A. 2022, Monthly Notices of the Royal Astronomical Society, Volume 510, Issue 4, pp.5743-5759, 510, 5743
Borucki, W. J., Koch, D., Basri, G., et al. 2010, Sci, 327, 977
Bowman, D. M. & Kurtz, D. W. 2018, Monthly Notices of the Royal Astronomical Society, 476, 3169
Breger, M., Breger, & M. 1990, DSSN, 2, 13
Breger, M., Lenz, P., Antoci, V., et al. 2005, A&A, 435, 955
Breger, M. & Montgomery, M., eds. 2000, Astronomical Society of the Pacific Conference Series, Vol. 210, Delta Scuti and Related Stars
Caldwell, D. A., Tenenbaum, P., Twicken, J. D., et al. 2020, Research Notes of the AAS, 4, 201
Creevey, O. L., Sordo, R., Pailler, F., et al. 2023, Astronomy and Astrophysics, 674, A26
Dupret, M.-A., Grigahcène, A., Garrido, R., et al. 2005, A&A, 435, 927
Gaia Collaboration, Vallenari, A., Brown, A. G., et al. 2023, Astronomy and Astrophysics, 674, A1
García Hernández, A., Pascual-Granado, J., Lares-Martiz, M., et al. 2024, Proceedings of the International Astronomical Union, 18, 239
Garrido, R., Garrido, & R. 2004, ESASP, 538, 117
Ginsburg, A., Sipőcz, B. M., Brasseur, C. E., et al. 2019, The Astronomical Journal, 157, 98
Grigahcène, A., Antoci, V., Balona, L., et al. 2010, The Astrophysical Journal Letters, 713, L192
Guzik, J. A., Kaye, A. B., Bradley, P. A., Cox, A. N., & Neuforge, C. 2000, ApJ, 542, L57
Han, T. & Brandt, T. D. 2023, The Astronomical Journal, 165, 71
Handberg, R., Lund, M. N., White, T. R., et al. 2021, The Astronomical Journal, 162, 170
Holdsworth, D. L., Cunha, M. S., Lares-Martiz, M., et al. 2024, Monthly Notices of the Royal Astronomical Society, 527, 9548
Huang, C. X., Vanderburg, A., Pál, A., et al. 2020a, Research Notes of the AAS, 4, 204
Huang, C. X., Vanderburg, A., Pál, A., et al. 2020b, RNAAS, 4, 206
Hubrig, S., Nesvacil, N., Schöller, M., et al. 2005, A&A, 440, L37
Hunt, E. L. & Reffert, S. 2024, Astronomy and Astrophysics, 686, A42
Kunimoto, M., Huang, C., Tey, E., et al. 2021, Research Notes of the AAS, 5, 234
Kurtz, D. W. 1982, MNRAS, 200, 807
Li, G., Reeth, T. V., Bedding, T. R., et al. 2019, MNRAS, 491, 3586
Lund, M. N., Handberg, R., Buzasi, D. L., et al. 2021, The Astrophysical Journal Supplement Series, 257, 53
Marques, J. P., Goupil, M. J., Lebreton, Y., et al. 2013, Astronomy & Astrophysics, 549, A74
Martínez-Vázquez, C. E., Salinas, R., Vivas, A. K., & Catelan, M. 2022, The Astrophysical Journal Letters, 940, L25
Mathis, S. & Zahn, J.-P. 2004, Astronomy and Astrophysics, 425, 229
McNamara, D. H. 2011, The Astronomical Journal, Volume 142, Issue 4, article id. 110, 22 pp. (2011)., 142, 110
Murphy, S. J. 2015, Monthly Notices of the Royal Astronomical Society, 453, 2569
Murphy, S. J., Hey, D., Reeth, T. V., & Bedding, T. R. 2019, Monthly Notices of the Royal Astronomical Society, 485, 2380
Nascimbeni, V., Piotto, G., Cabrera, J., et al. 2025, Astronomy & Astrophysics, Volume 694, id.A313, 19 pp., 694, A313
Niemczura, E., Smalley, B., & Pych, W. 2014, dapb
Ochsenbein, F., Bauer, P., & Marcout, J. 2000, Astronomy and Astrophysics Supplement Series, 143, 23
Palakkatharappil, D. B. & Creevey, O. L. 2023, A&A, 674, A146
Pamos Ortega, D., Hernández, A. G., Suárez, J. C., et al. 2022, Monthly Notices of the Royal Astronomical Society, 513, 374
Poro, A., Jafarzadeh, S. J., Harzandjadidi, R., et al. 2024, Research in Astronomy and Astrophysics, 24, 025011
Press, W. H. & Rybicki, G. B. 1989, ApJ, 338, 277
Rain, M. J., Carraro, G., Ahumada, J. A., et al. 2020, The Astronomical Journal, 161, 37
Rauer, H., Aerts, C., Cabrera, J., et al. 2025, Experimental Astronomy, Volume 59, Issue 3, id.26, 59, 26, cadence from PLATO compared to TESS (page 26)
Ricker, G. R., Winn, J. N., Vanderspek, R., et al. 2014, Journal of Astronomical Telescopes, Instruments, and Systems, 1, 014003
Rodríguez-Martín, J. E., García Hernández, A., Suárez, J. C., & Rodón, J. R. 2020, Monthly Notices of the Royal Astronomical Society, 498, 1700

[10] https://www.cosmos.esa.int/gaia
[11] https://www.cosmos.esa.int/web/gaia/dpac/consortium

Savitzky, A. & Golay, M. J. 1964, Analytical Chemistry, 36, 1627
Stassun, K. G., Oelkers, R. J., Paegert, M., et al. 2019, The Astronomical Journal, 158, 138
Stellingwerf, R. F., Stellingwerf, & F., R. 1979, ApJ, 227, 935
Suárez, J. C. & Goupil, M. J. 2008, Astrophysics and Space Science, 316, 155
Suárez, J. C., Goupil, M. J., & Morel, P. 2006, Astronomy & Astrophysics, 449, 673
Suárez, J. C., Garrido, R., & Goupil, M. J. 2006, Astronomy & Astrophysics, 447, 649
Uytterhoeven, K., Moya, A., Grigahcène, A., et al. 2011, Astronomy and Astrophysics, 534, A125
VanderPlas, J. T. 2018, The Astrophysical Journal Supplement Series, 236, 16
Walker, G., Matthews, J., Kuschnig, R., et al. 2003, Publications of the Astronomical Society of the Pacific, 115, 1023
Watson, C. L., Henden, A. A., & Price, A. 2006, The Society for Astronomical Sciences 25th Annual Symposium on Telescope Science. Held May 23-25, 2006, at Big Bear, CA. Published by the Society for Astronomical Sciences., p.47, 25, 47
Xiong, D. R., Deng, L., Zhang, C., & Wang, K. 2016, Monthly Notices of the Royal Astronomical Society, 457, 3163
Zahn, J.-P. 1992, Astronomy & Astrophysics, 265, 115
Ziaali, E., Bedding, T. R., Murphy, S. J., Reeth, T. V., & Hey, D. R. 2019, Monthly Notices of the Royal Astronomical Society, 486, 4348
Zwintz, K., Reese, D. R., Neiner, C., et al. 2019, A&A, 627, A28

Appendix A: Tables

Table A.1. TIC parameters included in SPATO. For each parameter x, the corresponding uncertainty is listed as e_x. Gaia identifier corresponds to Data Release 2. Nevertheless, for our sample the identifier was the same as Gaia DR3, and the cross-match with either identifier returned the same output.

Parameter	Description
id	TIC identifier
GAIA	DR2 Gaia identifier
objType	Object type
dec	Declination (deg)
ra	Right Ascension (deg)
gallong	Galactic longitude (deg)
gallat	Galactic latitude (deg)
V_mag, e_Vmag	Johnson V magnitude and uncertainty
GAIAmag, e_GAIAmag	Gaia G magnitude and uncertainty
Teff, e_Teff	Effective temperature (K) and uncertainty
logg, e_logg	Surface gravity (dex) and uncertainty
MH, e_MH	Metallicity and uncertainty
rho, e_rho	Stellar mean density and uncertainty
mass, e_mass	Stellar mass ($M_\odot$) and uncertainty
rad, e_rad	Stellar radius ($R_\odot$) and uncertainty
lum, e_lum	Stellar luminosity ($L_\odot$) and uncertainty

Table A.2. Gaia DR3 and auxiliary parameters included in the catalogue for the enriched sample. Upper and lower indices correspond to the quoted uncertainties for each parameter when available. FLAME and GSP-Phot are two pipelines for parameter estimation used by Gaia that are described in section 3.1.

Parameter	Description
source_id	Gaia DR3 source identifier
ra, dec	Right Ascension and Declination (deg)
l, b	Galactic longitude and latitude (deg)
mg_gspphot, mg_gspphot_upper/lower	Absolute G magnitude (GSP-Phot) and uncertainties
teff_gspphot, teff_gspphot_upper/lower	Effective temperature (K, GSP-Phot) and uncertainties
teff_esphs, teff_esphs_uncertainty	Effective temperature (K, ESP-HS) and uncertainties
logg_gspphot, logg_gspphot_upper/lower	Surface gravity (dex, GSP-Phot) and uncertainties
distance_gspphot	Distance estimate (pc, GSP-Phot)
radius_gspphot, radius_gspphot_upper/lower	Stellar radius ($R_\odot$, GSP-Phot) and uncertainties
mh_gspphot, mh_gspphot_upper/lower	Metallicity [M/H] (GSP-Phot) and uncertainties
lum_flame, lum_flame_upper/lower	Luminosity ($L_\odot$, FLAME) and uncertainties
radius_flame, radius_flame_upper/lower	Stellar radius ($R_\odot$, FLAME) and uncertainties
mass_flame, mass_flame_upper/lower	Stellar mass ($M_\odot$, FLAME) and uncertainties
binary_flag	Binary star flag
best_class_name	Best variability class (classifier)
best_class_score	Confidence score of classification
class_description	Description of variability class
best_rotation_period	Best estimate of stellar rotation period (d)
frequency1	Main oscillation frequency (d^{-1})
amplitude_g_freq1	Amplitude in G band at frequency1 (mmag)
amplitude_g_freq1_harm2/3	Amplitudes of harmonic 2 and 3 (mmag)
vsini_esphs, vsini_esphs_uncertainty	Projected rotational velocity ($v \sin i$) and uncertainty

Table A.3. Flux retrieved from each light-curve analysis pipeline.

Pipeline	Flux column	Documentation
TASOC	FLUX_CORR	https://archive.stsci.edu/hlsp/tasoc
SPOC	PDCSAP_FLUX	https://archive.stsci.edu/hlsp/tess-spoc
QLP	SAP_FLUX	https://archive.stsci.edu/hlsp/qlp
TGLC	CAL_PSF_FLUX	https://archive.stsci.edu/hlsp/tglc
ELEANOR	CORR_FLUX	https://archive.stsci.edu/hlsp/gsfc-eleanor-lite
CDIPS	PCA1	https://archive.stsci.edu/hlsp/cdips

Table A.4. Description of the headers included in the frequency analysis catalog.

Header	Description
f_ID	Identifier for each star frequency in order of amplitude
ID	Identifier for frequencies that were not interpreted as an alias due to the window function
id_tess	TESS Input Catalog (TIC) identifier
author	Author or pipeline responsible for the analysis
exptime	Exposure time of the observations (s)
Sector	TESS observing sector
Freqs	Detected oscillation frequencies (cycles per day)
Amps	Amplitudes corresponding to the detected frequencies (ppm)
Phases	Phases associated with the detected frequencies
Amplitude 1-sigma error (ppm)	Uncertainty of the amplitude measurements
Frequency 1-sigma error (c/d)	Uncertainty of the frequency measurements
Phase 1-sigma error (c/d)	Uncertainty of the phase measurements
SNR/FAP	Signal-to-noise ratio or false alarm probability
rms	Root mean square of the residuals after prewhitening
linear_combination	Linear Combination of frequencies wich matches the frequency
Window_Alias	Alias frequencies related to the spectral window
Theoretical Alias_Amp	Expected amplitude of theoretical alias frequencies

Appendix B: Figures

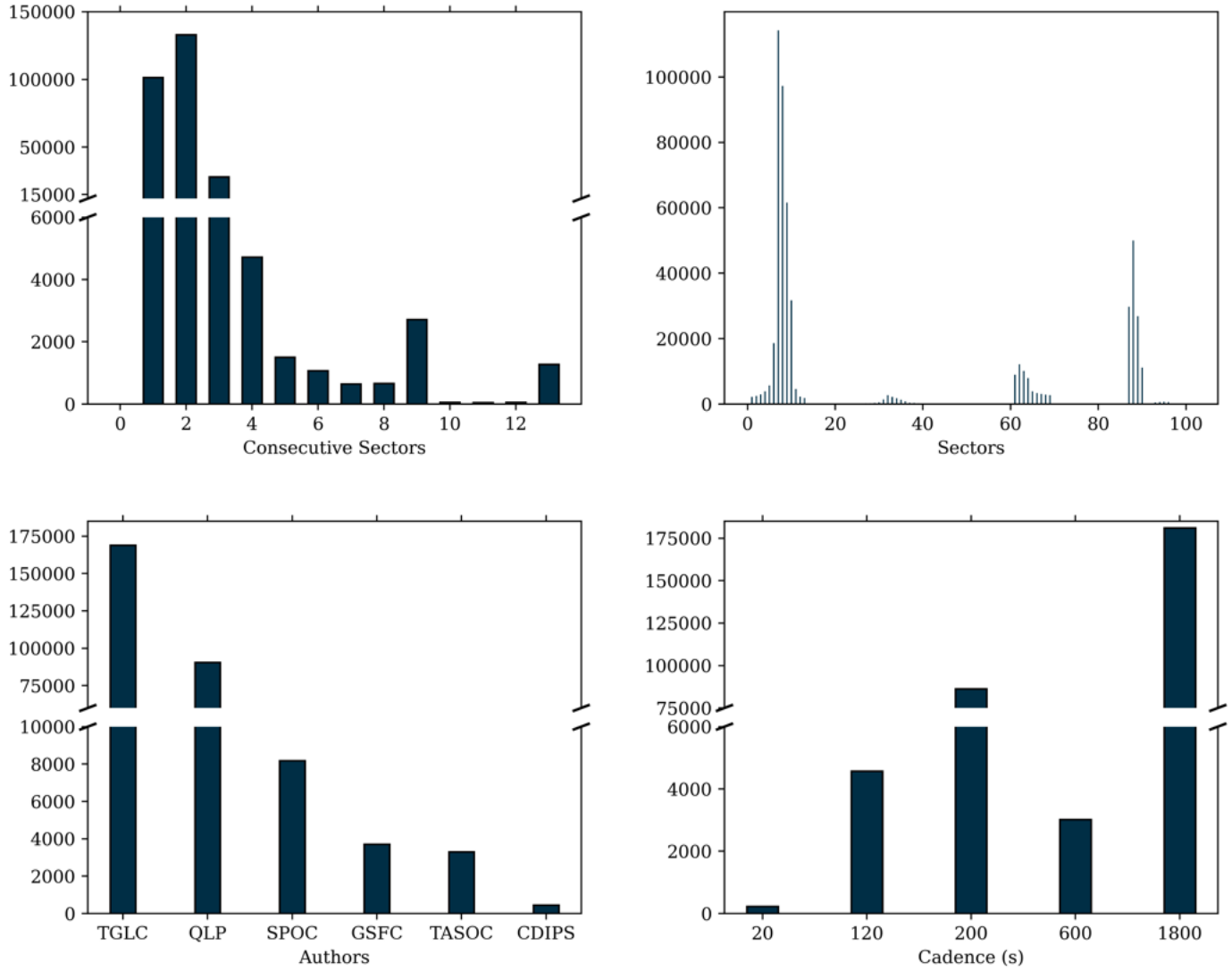

Fig. B.1. *Top left*: Histogram of the number of light curves as a function of the number of consecutively stitched TESS sectors. *Top right*: Distribution of the number of TESS sectors included in the processed light curves, whether stitched or not. *Bottom left*: Histogram of light curves grouped by the pipeline from which they were obtained. *Bottom right*: Histogram of light curves as a function of their cadence.

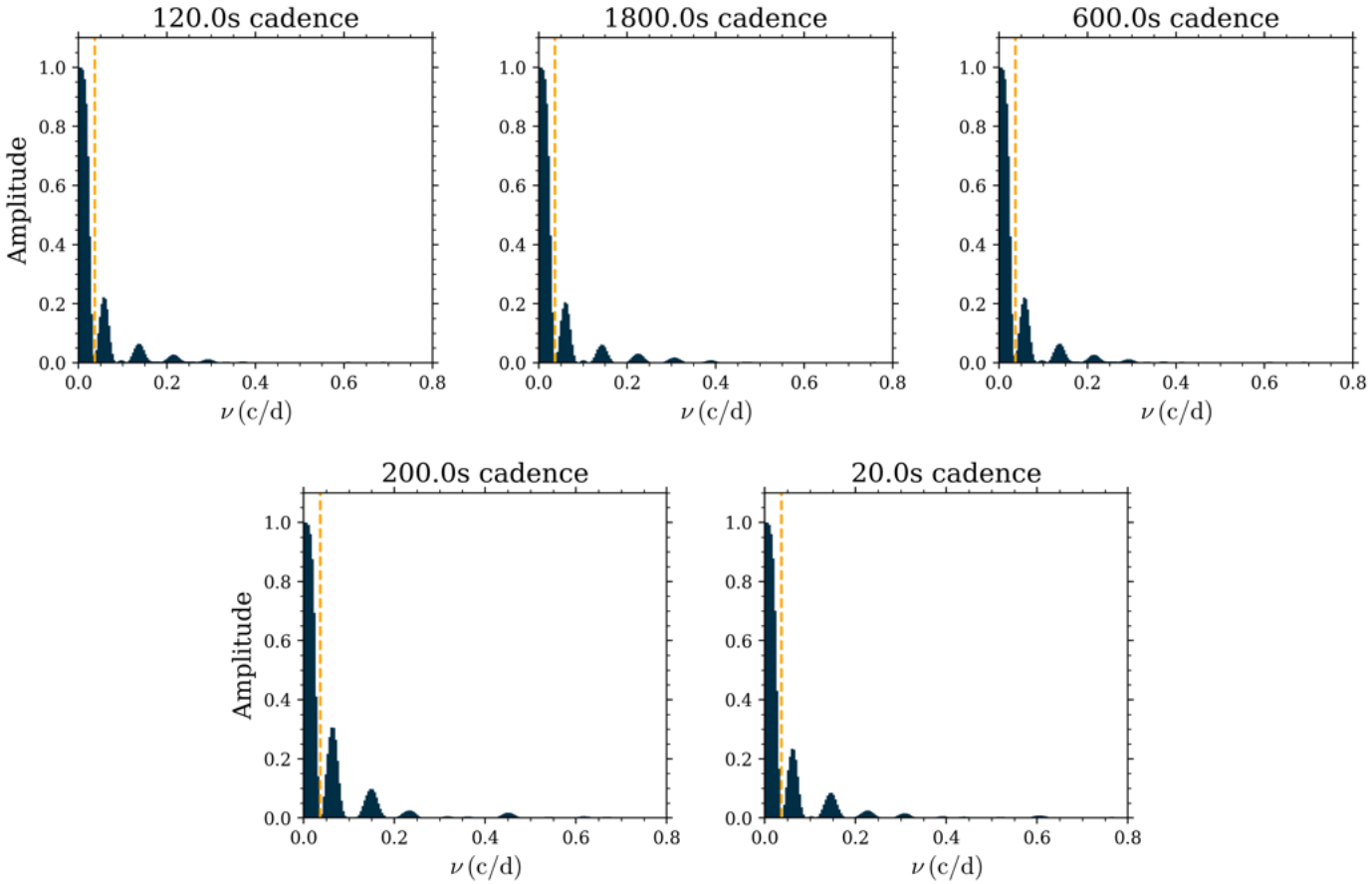

Fig. B.2. Spectral window function $W(f)$ for single-sector light curves, computed as the Fast Lomb-Scargle periodogram (the same method employed by *MultiModes*) of a unit-normalized flux. The Rayleigh frequency f_R is indicated by the orange dashed line.

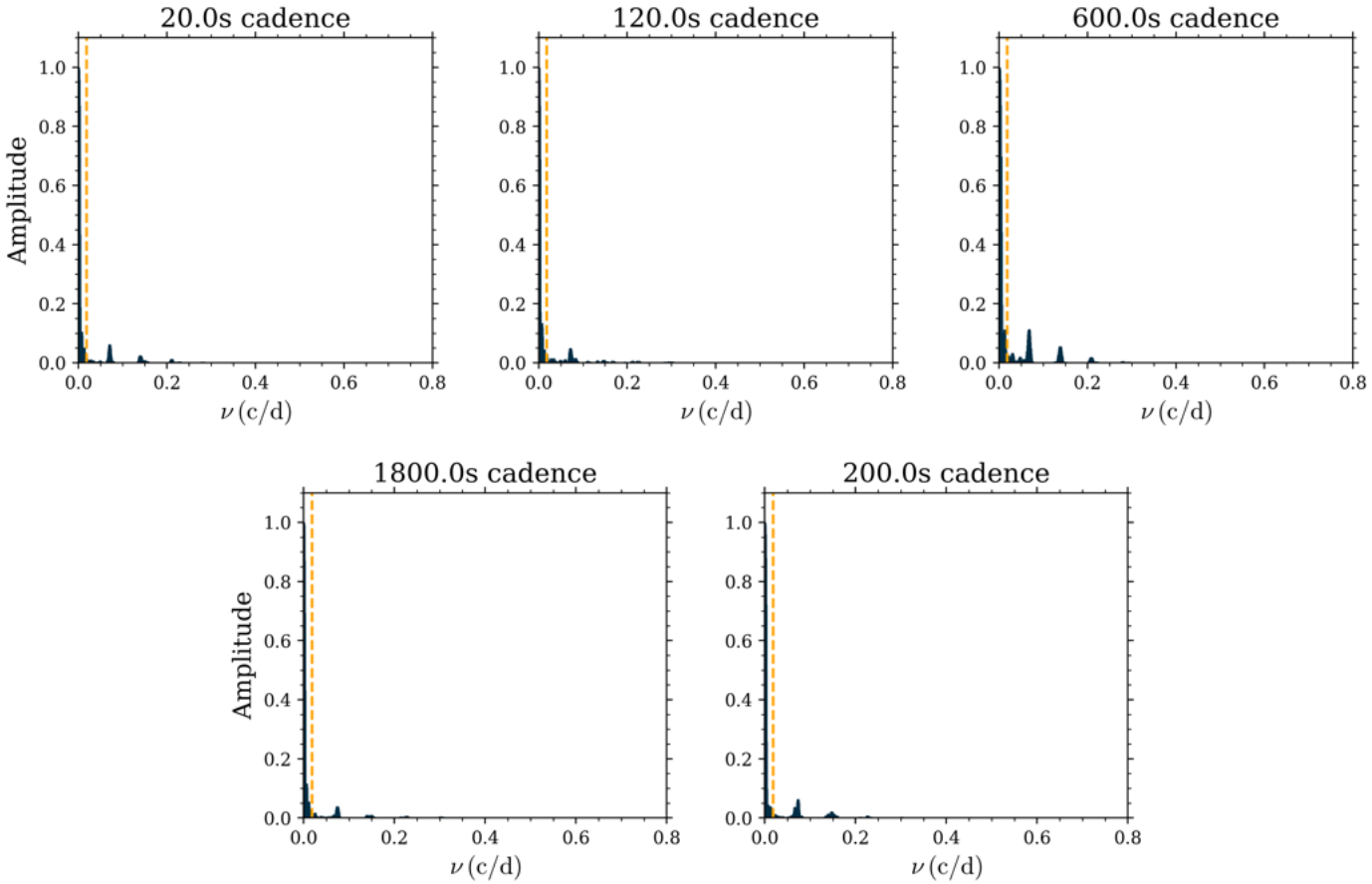

Fig. B.3. Spectral window function $W(f)$ for multi-sector light curves, computed as the Fast Lomb-Scargle periodogram (the same method employed by *MultiModes*) of a unit-normalized flux. The Rayleigh frequency f_R is indicated by the orange dashed line.

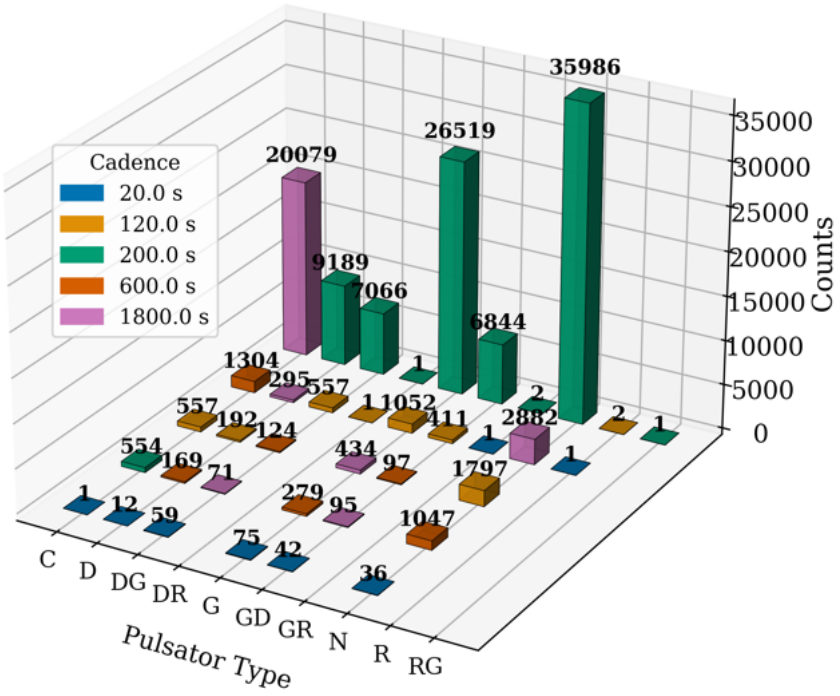

Fig. B.4. Histogram of the initial sample pulsating stars grouped by the cadence of their light curves, where "D" denotes δ Scuti, "G" γ Doradus, "R" roAp, a two-letter combination "XY" indicates a hybrid pulsator with primary type "X", and "C" constant stars. 1800s cadence shown here have, at least, 3 consecutive sectors.